physica status solidi b
www.pss-b.com
basic solid state physics

Elastic and piezoelectric fields in quantum wire semiconductor structures – A boundary integral equation analysis

E. Pan[1], **J. D. Albrecht**[2], and **Y. Zhang**[1]

[1] University of Akron, Akron, OH 44039, USA
[2] Air Force Research Laboratory, Wright-Patterson Air Force Base, OH 45433, USA

Received 10 October 2006, revised 20 December 2006, accepted 1 February 2007
Published online 7 March 2007

PACS 62.40.+i, 68.65.La, 77.65.Ly

This paper presents a rigorous analysis on the elastic and piezoelectric fields in quantum wire (QWR) semiconductor structures using the accurate boundary integral equation method. The materials modelled include both zincblende and wurtzite III–V semiconductors, and both the well-accepted inclusion and structural inhomogeneity models are discussed. While the difference in the strain field between the inclusion and inhomogeneity models is consistent with previously published results, within about 10%, the difference in the induced piezoelectric fields between these two models can be very large, sometimes even with different signs (for zincblende semiconductors). The electric field distribution in polygonal QWRs with different sides is also studied and it is found that the electric field in triangular and square QWRs can be very different from the fields in polygonal QWRs with more than four sides. These findings should provide important considerations and trend analyses for both growth and modelling associated with QWR semiconductor structures.

phys. stat. sol. (b) **244**, No. 6, 1925–1939 (2007) / **DOI** 10.1002/pssb.200642513

Original Paper

phys. stat. sol. (b) **244**, No. 6, 1925–1939 (2007) / **DOI** 10.1002/pssb.200642513

Elastic and piezoelectric fields in quantum wire semiconductor structures – A boundary integral equation analysis

E. Pan[*, 1], **J. D. Albrecht**[2], and **Y. Zhang**[1]

[1] University of Akron, Akron, OH 44039, USA
[2] Air Force Research Laboratory, Wright-Patterson Air Force Base, OH 45433, USA

Received 10 October 2006, revised 20 December 2006, accepted 1 February 2007
Published online 7 March 2007

PACS 62.40.+i, 68.65.La, 77.65.Ly

This paper presents a rigorous analysis on the elastic and piezoelectric fields in quantum wire (QWR) semiconductor structures using the accurate boundary integral equation method. The materials modelled include both zincblende and wurtzite III–V semiconductors, and both the well-accepted inclusion and structural inhomogeneity models are discussed. While the difference in the strain field between the inclusion and inhomogeneity models is consistent with previously published results, within about 10%, the difference in the induced piezoelectric fields between these two models can be very large, sometimes even with different signs (for zincblende semiconductors). The electric field distribution in polygonal QWRs with different sides is also studied and it is found that the electric field in triangular and square QWRs can be very different from the fields in polygonal QWRs with more than four sides. These findings should provide important considerations and trend analyses for both growth and modelling associated with QWR semiconductor structures.

1 Introduction

Quantum well (QW), quantum wire (QWR), and quantum dot (QD) semiconductor nanostructures with their associated degrees of quantum carrier confinement can be tailored to address the electron energy state requirements of future electronic and optoelectronic devices [1]. Frequently, the nanostructures under consideration are formed through heteroepitaxy. Therefore the lattice misfit conditions, or pseudomorphically induced strain fields, are central to determining and engineering the electronic states of the quantum mechanical system through modifications to the electronic structure (changes in band gap and effective mass) of the constituent materials and direct modifications to the confining potential (changes in lattice polarization). It is crucial from a device modeling perspective that the induced strain and electric fields in the nanostructure be modeled accurately and efficiently.

This study is focused on the elastic and piezoelectric field prediction in strained QWR structures. From the field of continuum mechanics, we have a first approximation, the well-known Eshelby inclusion method [2–4], which has been successfully applied to study the induced strain/electric fields in many structures. In the Eshelby treatment the lattice misfit between the QWR and substrate (or matrix) is imposed but the QWR material is assumed to be the same as its substrate [5–10]. The advantage of the Eshelby inclusion method is its simplicity and the induced elastic and electric fields can be found analytically for both 2D QWR and 3D QD cases.

[*] Corresponding author: e-mail: pan2@uakron.edu, Phone: 330-972-6739, Fax: 330-972-6020

Recently, the relative accuracy and underlying assumptions of the inclusion model have come under scrutiny. A structural inhomogeneity model which considers the relevant and different elastic material properties present in realistic QWR/QD structures was developed [11, 12] and compared with the inclusion method. In our previous work [12], the issue of the homogeneous inclusion vs. structural inhomogeneity in the context of strained QWRs was studied in detail for purely elastic zincblende semiconductors using the boundary integral equation method (BEM). Numerical examples were given for InAs/GaAs QWRs in both (001) and (111) growth directions for square and trapezoidal QWR cross-sections. Several results were obtained, including: (i) As expected, the strain fields predicted in the substrate but far away from the QWR were very similar for both models because the internal details of the wire composition are irrelevant to the far-field response. (ii) For points within or near to the QWR, the variation in predicted field strengths between the models can be as high as 10% for these materials and geometries. (iii) Although the singular behavior present near the sharp corners of the QWR looks similar in form for both models, the amplitudes of the singularity are significantly different in some cases.

A more complete picture of the strain effects on quantum heterostructures is gained by extending the calculations to include any spontaneous and piezoelectric polarizations which will directly change the local electrostatic potential. So far, the differences present in the induced polarization electric fields as obtained by both the homogeneous inclusion and structural inhomogeneity models has not been reported in the literature, which is the main motivation of this study. In this paper we therefore develop a simple BEM formulation to investigate the elastic and electric fields present in QWR semiconductor structures. Our BEM algorithm is based on constant-element discretization with analytical kernel function integration. The corresponding BEM routine is then applied to systems composed of InAs QWRs in (001)- and (111)-orientated GaAs and of InN QWRs in (0001)- and (1000)-oriented wurtzite AlN ((1000) means along the polar direction, i.e., a direction normal to the (0001)-axis). The QWRs considered are polygonal and the formalism is sufficiently general to include the possibility of irregular shapes. While our BEM program includes the simple homogeneous inclusion as a limiting case, the Eshelby inclusion solution developed before [12] is also applied to check the accuracy of our BEM program. Though the elastic strain features from both the inclusion and inhomogeneity models are consistent with previous reports [11, 12], we will show that the induced electric fields can be very different. The main conclusion is that the inhomogeneous material properties need to be taken into account to reliably predict the induced electric fields in strained QWRs.

This paper is organized as follows. In Section 2, we describe the problem to be solved, along with the associated basic equations. In Section 3, the BEM and the corresponding constant-element discretization is presented. Then in Sections 4 and 5 we present various numerical examples and draw conclusions.

2 Problem description and basic equations

A general QWR problem is illustrated by Fig. 1, where, to facilitate our discussion, we have defined the following extended strain:

$$\gamma_{Ij} = \begin{cases} \gamma_{Ij}, & I = i = 1, 2, 3, \\ -E_j, & I = 4. \end{cases} \tag{1}$$

In Eq. (1), γ_{ij} is the total elastic strain tensor and E_i the i-th Cartesian component of the total electric field, which are related to the total elastic displacement u_i and total electric potential ϕ in the usual way by

$$\gamma_{ij} = \frac{1}{2}\left(\frac{\partial u_i}{\partial x_j} + \frac{\partial u_j}{\partial x_i}\right), \qquad E_j = -\frac{\partial \phi}{\partial x_j}. \tag{2}$$

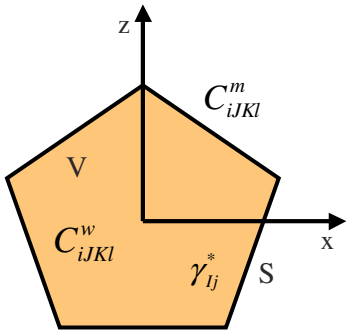

Fig. 1 (online colour at: www.pss-b.com) An arbitrarily shaped polygon QWR inclusion/inhomogeneity with eigenstrain γ^*_{Ij} in an anisotropic substrate.

The total extended strain is the sum of

$$\gamma_{Ij} = \gamma^e_{Ij} + \gamma^*_{Ij}, \tag{3}$$

where γ^*_{Ij} is the extended eigenstrain in the QWR (Fig. 1), and γ^e_{Ij} the extended strain that appears in the generalized constitutive relation [12] as

$$\sigma_{iJ} = C_{iJKl}\gamma^e_{Kl} \tag{4a}$$

or

$$\sigma_{iJ} = C_{iJKl}(\gamma_{Kl} - \chi\gamma^*_{Kl}), \tag{4b}$$

where summation over repeated indices *K, l* is implied and χ is equal to one if the observation point is within the QWR domain *V* and zero outside (Fig. 1). It is clear that, in this paper, the contribution from the spontaneous polarization is not considered. Furthermore, the corresponding material properties belong to the QWR and substrate should be used in Eq. (4) when calculating the induced extended stress, which is defined as

$$\sigma_{iJ} = \begin{cases} \sigma_{ij}, & J = j = 1, 2, 3, \\ D_i, & J = 4, \end{cases} \tag{5}$$

where σ_{ij} and D_i are the stress and electric displacement, respectively. In Eq. (4), the general moduli are defined as

$$C_{iJKl} = \begin{cases} C_{ijkl}, & J, K = j,\ k = 1, 2, 3 \\ e_{lij}, & J = j = 1,\ 2,\ 3, \quad K = 4 \\ e_{ikl}, & J = 4, \quad K = k = 1, 2, 3 \\ -\varepsilon_{il}, & J = K = 4 \end{cases} \tag{6}$$

with C_{ijlm}, e_{ijk} and ε_{ij} being the elastic moduli, piezoelectric coefficients, and dielectric constants, respectively. For completeness, we further define the extended displacement as

$$u_I = \begin{cases} u_i, & I = i = 1, 2, 3, \\ \phi, & I = 4. \end{cases} \tag{7}$$

Let us assume that the general misfit strain γ^*_{Ij} (I = 1, 2, 3, 4 and j = 1, 2, 3) is uniform within the QWR domain and is zero outside (Fig. 1). The interface between the QWR and matrix is labeled *s*. We

also denote C^w_{iJKl} and C^m_{iJKl} as the general moduli of the QWR and matrix materials, respectively (Fig. 1). For the homogeneous inclusion problem, $C^w_{iJKl}=C^m_{iJKl}$. If there is no body force and no electric charge within the QWR system, one can easily show that, for the matrix domain,

$$C^m_{iJKl}u^m_{K,li}=0\,, \tag{8}$$

and for the QWR domain,

$$C^w_{iJKl}u^w_{K,li}=C^w_{iJKl}\gamma^*_{Kl,i}\,. \tag{9}$$

It is clear that the right hand side of Eq. (9) is equivalent to a body force defined as

$$f^{(w)}_J=-C^w_{iJKl}\gamma^*_{Kl,i}\,, \tag{10}$$

which is also called the equivalent body force of the eigenstrain [4, 9]. This equivalent body force will be employed in the next section to convert the contribution of the eigenstrain to a boundary integral along the interface of the QWR and its substrate. Again, the superscripts *m* and *w* denote quantities associated with the matrix and QWR, respectively.

3 Boundary integral equations and constant-element discretization

To solve the problem in Fig. 1, we apply the BEM to both the QWR and its matrix/substrate. The boundary integral formulation can be expressed as [11, 12]

$$b_{IJ}(\boldsymbol{X})\,u^m_J(\boldsymbol{X})=\int_S [U^m_{IJ}(\boldsymbol{X},\boldsymbol{x})\,t^m_J(\boldsymbol{x})-T^m_{IJ}(\boldsymbol{X},\boldsymbol{x})\,u^m_J(\boldsymbol{x})]\,\mathrm{d}s(\boldsymbol{x}) \tag{11}$$

for the matrix, and

$$b_{IJ}(\boldsymbol{X})\,u^w_J(\boldsymbol{X})=\int_S [U^w_{IJ}(\boldsymbol{X},\boldsymbol{x})\,(t^w_J(\boldsymbol{x})+f^w_J(\boldsymbol{x}))-T^w_{IJ}(\boldsymbol{X},\boldsymbol{x})\,u^w_J(\boldsymbol{x})]\,\mathrm{d}s(\boldsymbol{x}) \tag{12}$$

for the QWR.

In Eqs. (11) and (12) t_J and u_J are the traction and displacement components, and $\boldsymbol{x}$ and $\boldsymbol{X}$ are the coordinates of the field and source points, respectively. The coefficients b_{IJ} equal δ_{IJ} if $\boldsymbol{X}$ is an interior point and $\delta_{IJ}/2$ at a smooth boundary point. For points at complicated geometry locations, these coefficients can be determined by the rigid-body motion method [15]. Furthermore, in Eq. (12), f^w_J is the traction induced by the misfit eigenstrain inside the QWR, which is given by Eq. (10).

The Green's functions U_{IJ} and T_{IJ} in Eqs. (11) and (12) are taken to be the special 2D Green's functions for the full plane [16, 17]. The indices *I* and *J* indicate the *J*-th Green's (general) displacement/traction (at $\boldsymbol{x}$) in response to a (general) line-force in the *I*-th direction (applied at $\boldsymbol{X}$). Note that the Green's functions are in exact closed form, and thus their integration over constant elements can be carried out exactly as discussed below. This is computationally desirable as it is very efficient and accurate for the calculation.

Employing constant-value elements, we divide the boundary (interface) into *N* segments with the *n*-th element being labeled as s_n. The constant values u_{Jn} and t_{Jn} on the *n*-th element equal to those values at the center of the element. Under this assumption, the boundary integral Eqs. (11) and (12) for the surrounding matrix and QWR domains are reduced to the following algebraic equations

$$b_{IJ}u^m_J+\sum_{n=1}^{N}\left(\int_{s_n}T^m_{IJ}\,\mathrm{d}s\right)u^m_{Jn}=\sum_{n=1}^{N}\left(\int_{s_n}U^m_{IJ}\,\mathrm{d}s\right)t^m_{Jn}\,, \tag{13}$$

and

$$b_{LJ}u_J^w + \sum_{n=1}^{N}\left(\int_{s_n} T_{LJ}^w \,\mathrm{d}s\right) u_{Jn}^w = \sum_{n=1}^{N}\left(\int_{s_n} U_{LJ}^w \,\mathrm{d}s\right)(t_{Jn}^w + C_{pJKl}^w \gamma_{Kl}^* n_p)\,. \tag{14}$$

The difference between Eqs. (13) and (14) is the traction induced by the misfit eigenstrain inside the QWR in Eq. (14).The remaining problem is to find the suitable Green's functions U_{LJ} and T_{LJ}, as well as their integrals over each element s_n, which are the kernel functions in these equations. Next we will present the analytical integration of these Green's functions over an arbitrary constant element.

To carry out the line integration of the Green's functions over a constant element, we first look at the Green's functions in Eqs. (13) and (14). They can be expressed as [9, 16, 17]

$$U_{LJ}(\boldsymbol{x}, \boldsymbol{X}) = \frac{1}{\pi}\,\mathrm{Im}\left\{A_{JR}\,\ln(z_R - s_R)\,A_{IR}\right\}, \tag{15}$$

$$T_{LJ}(\boldsymbol{x}, \boldsymbol{X}) = \frac{1}{\pi}\,\mathrm{Im}\left\{B_{JR}\,\frac{p_R n_1 - n_3}{z_R - s_R}\,A_{IR}\right\}, \tag{16}$$

where "Im" stands for the imaginary part of the complex value, A_{LJ} and B_{LJ} are two constant matrices related only to the material properties [16], n_1 and n_3 are the unit outward normal components projected along the x- and z-directions, p_R ($R = 1, 2, 3, 4$) are the Stroh eigenvalues, and $z_R = x + p_R z$ and $s_R = X + p_R Z$ are the field and source points, respectively.

To form an arbitrary element, we define a generic line segment representing any constant element along the interface in the (x,z)-plane, starting from point 1 (x_1, z_1) and ending at point 2 (x_2, z_2). In terms of the parameter t ($0 \le t \le 1$), any constant line element can be parameterized as

$$x = x_1 + (x_2 - x_1)\,t\,, \qquad z = z_1 + (z_2 - z_1)\,t\,. \tag{17}$$

The outward normal components along the line segment are constant, given by

$$n_1 = (z_2 - z_1)/l\,, \qquad n_3 = -(x_2 - x_1)/l\,, \tag{18}$$

where l is the length of the line segment and the elemental length is $\mathrm{d}s = l\,\mathrm{d}t$.

It is observed that Eqs. (11) and (12) consist of only two different integrals possessing the following analytic results. The first integral is a function of the source point $\boldsymbol{X} = (X, Z)$ and is expressed in parameterized form by

$$h_R(X, Z) \equiv \int_0^1 \ln(z_R - s_R)\,\mathrm{d}t\,, \tag{19}$$

which can be expanded as

$$h_R(X, Z) = \int_0^1 \ln\{[(x_2 - x_1) + p_R(z_2 - z_1)]\,t + [(x_1 + p_R z_1) - s_R]\}\,\mathrm{d}t\,, \tag{20}$$

and can immediately be evaluated to the following closed form:

$$h_R(X, Z) = \frac{(x_1 + p_R z_1) - s_R}{(x_2 - x_1) + p_R(z_2 - z_1)}\ln\left[\frac{x_2 + p_R z_2 - s_R}{x_1 + p_R z_1 - s_R}\right] + \ln[x_2 + p_R z_2 - s_R] - 1\,. \tag{21}$$

Similarly, we take the second integral as

$$g_R(X,Z) \equiv \int_0^1 \frac{\mathrm{d}t}{z_R - s_R}, \tag{22}$$

which upon evaluation leads to

$$g_R(X,Z) = \frac{1}{(x_2 - x_1) + p_R(z_2 - z_1)} \ln\left[\frac{x_2 + p_R z_2 - s_R}{x_1 + p_R z_1 - s_R}\right]. \tag{23}$$

Therefore, based on the constant-element discretization the two boundary integral Eqs. (11) and (12) for the QWR and matrix/substrate can be cast into a system of algebraic equations for the interface points. In matrix form, they can be expressed as

$$\boldsymbol{U}^w \boldsymbol{t}^w - \boldsymbol{T}^w \boldsymbol{u}^w = \boldsymbol{f}^w, \tag{24}$$

$$\boldsymbol{U}^m \boldsymbol{t}^m - \boldsymbol{T}^m \boldsymbol{u}^m = 0, \tag{25}$$

where the coefficient matrices $\boldsymbol{U}$ and $\boldsymbol{T}$ are the exact integrals of Green's functions on each constant element given in Eqs. (21) and (23), and $\boldsymbol{u}$ and $\boldsymbol{t}$ are the general displacement and traction vectors at the center of each element. The right-hand side term $\boldsymbol{f}^w$ in Eq. (24) is the general equivalent force corresponding to the misfit eigenstrain within the QWR.

We assume that the matrix and QWR are perfectly bonded along the interface s, that is, the continuity conditions $\boldsymbol{u}^m = \boldsymbol{u}^w$ and $\boldsymbol{t}^m = -\boldsymbol{t}^w$ hold. Then the number of unknowns is identical to the number of equations and all the nodal (general) displacements and tractions can be determined. Furthermore, making use of the Somigliana identity, the displacement at any location within the QWR can be easily obtained in general as

$$b_{IJ} u_J^w + \sum_{n=1}^{N} \left(\int_{s_n} T_{IJ}^w \, \mathrm{d}\Gamma \right) u_{Jn}^w = \sum_{n=1}^{N} \left(\int_{s_n} U_{IJ}^w \, \mathrm{d}\Gamma \right) (t_{Jn}^w + C_{pJKl}^w \gamma_{Kl}^* n_p), \tag{26}$$

where the last force term exists exclusively for the QWR domain. Furthermore, utilizing Eqs. (1)–(5), we can calculate the induced elastic and electric fields at any point within the matrix or QWR.

In summary, we have derived exact boundary integral equations for the QWR and matrix domains by constant-element discretization along their interface. These equations can be used to find the elastic and piezoelectric responses along the interface and at any location within the QWR and its surrounding matrix. Applications of these solutions to QWR systems are discussed in the next section.

Table 1 Material properties and misfit strains in InAs(001)/GaAs(001) [18, 19].

	InAs	GaAs
$C_{11} = C_{22} = C_{33}$ (GPa)	83.29	118.8
$C_{12} = C_{13} = C_{23}$	45.26	53.8
$C_{44} = C_{55} = C_{66}$	39.59	59.4
$e_{14} = e_{25} = e_{36}$ (C/m^2)	−0.0456	−0.16
$\varepsilon_{11} = \varepsilon_{22} = \varepsilon_{33}$ (10^{-9}C^2/Nm^2)	0.1345808	0.110675
$\gamma_{11}^* = \gamma_{22}^* = \gamma_{33}^*$	0.07	

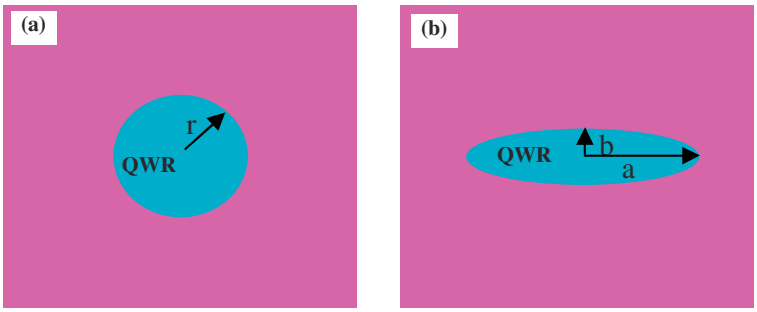

Fig. 2 (online colour at: www.pss-b.com) A circle QWR of radius $r = 10$ nm in an infinite substrate (a), and an ellipse QWR with length of the semi-major axis $a = 20$ nm in horizontal x-direction and the semi-minor axis $b = 5$ nm in vertical z-direction in an infinite substrate in (b).

4 Numerical examples

Numerical examples are developed in this section for two QWR material systems: One is the case of InAs wires in GaAs with (001)- and (111)-oriented substrates, and the other case is for InN wires buried in AlN with (1000)- and (0001)-orientations. Both the inclusion and inhomogeneity models are studied. For the corresponding inclusion model, the QWR materials take the material constants of their surrounding matrix but retain their misfit strain conditions. The material properties and eigenstrains within the QWR in the material coordinates are listed in Tables 1 and 2 [18, 19].

For InAs(111) and GaAs(111), the coordinate x-axis is along $[11\bar{2}]$, y-axis along $[\bar{1}10]$, and z-axis along [111] directions of the crystalline [19]. Their material properties can be obtained by coordinate rotations [19]. For InN (1000) and AlN (1000), the material properties can be obtained by simply switching the coordinate directions (between x and z).

4.1 Example 1. Circular and elliptic QWRs

The first example is for circular and elliptic QWRs in an infinite substrate (Fig. 2). For this case, exact solutions can be obtained for both the inclusion and inhomogeneity models.

Tables 3–6 compare the strain and electric fields inside both the circular and elliptic QWRs treated as inclusions and inhomogeneities (Fig. 2), using the material properties and eigenstrains listed in Tables 1

Table 2 Material properties and misfit strains in InN(0001)/AlN (0001) [18, 19].

	InN	AlN
$C_{11} = C_{22}$ (GPa)	223.0	396.0
C_{33}	224.0	373.0
C_{12}	115.0	137.0
$C_{13} = C_{23}$	92.0	108.0
$C_{44} = C_{55}$	48.0	116.0
C_{66}	54.0	129.5
$e_{15} = e_{24}$ (C/m^2)	−0.22	−0.48
$e_{31} = e_{32}$	−0.57	−0.58
e_{33}	0.97	1.55
$\varepsilon_{11} = \varepsilon_{22}$ (10^{-12} C^2/Nm^2)	132.81	79.686
ε_{33}	132.81	97.372
$\gamma^*_{11} = \gamma^*_{22}$	0.1357	
γ^*_{33}	0.1267	

Table 3 Strains in inclusion GaAs(001) and inhomogeneity InAs(001)/GaAs(001).

		inclusion	inhomogeneity	relative error (%)
circle	$\gamma_{xx} = \gamma_{zz}$	0.0612	0.0566	9
ellipse	γ_{xx}	0.0208	0.0134	55
	γ_{zz}	0.1058	0.1133	7

Table 4 Strains in inclusion GaAs(111) and inhomogeneity InAs(111)/GaAs(111).

		inclusion	inhomogeneity	relative error (%)
circle	γ_{xx}	0.0596	0.0551	8
	γ_{zz}	0.0543	0.5000	9
	$2\gamma_{xz}$	−0.0149	−0.0145	2
	E_x ($\times 10^7$ V/m)	4.020	0.2738	1368
	E_z ($\times 10^7$ V/m)	−2.843	−0.1936	1368
ellipse	γ_{xx}	0.0260	0.0196	33
	γ_{zz}	0.0829	0.0861	4
	$2\gamma_{xz}$	−0.0081	−0.0075	9
	E_x ($\times 10^7$ V/m)	1.235	0.4773	176
	E_z ($\times 10^7$ V/m)	−9.770	2.074	571

Table 5 Strain in an inclusion AlN(0001) and inhomogeneity InN(0001)/AlN(0001).

		inclusion	inhomogeneity	relative error (%)
circle	γ_{xx}	0.1184	0.1063	11
	γ_{zz}	0.0984	0.0876	12
	E_z ($\times 10^7$ V/m)	−47.05	−42.65	10
ellipse	γ_{xx}	0.0515	0.0310	66
	γ_{zz}	0.1555	0.1746	11
	E_z	−159.0	−130.1	22

Table 6 Strain in an inclusion AlN(1000) and inhomogeneity InN(1000)/AlN(1000).

		inclusion	inhomogeneity	relative error (%)
circle	γ_{xx}	0.0984	0.0876	12
	γ_{zz}	0.1184	0.1063	11
	E_x ($\times 10^7$ V/m)	−47.05	−42.65	10
ellipse	γ_{xx}	0.0403	0.0223	81
	γ_{zz}	0.1797	0.2008	11
	E_x ($\times 10^7$ V/m)	2.435	2.780	12

and 2. We point out that for these QWR shapes, the induced fields inside the QWR are uniform for both models. These results can be obtained using the analytical solution for the QWR inclusion problem [9], combined with the Eshelby inhomogeneity method [2–4]. Furthermore, we have also used our BEM formulation presented above for these models. In doing so, we have mutually checked our analytical and numerical solutions.

It is observed from Tables 3–6 that the relative error, defined as (inclusion solution – inhomogeneity solution)/(inhomogeneity solution), for the strain (the large z-component γ_{zz} in the ellipse case) between the inclusion and inhomogeneity models is generally around 10%, which is consistent with the recent

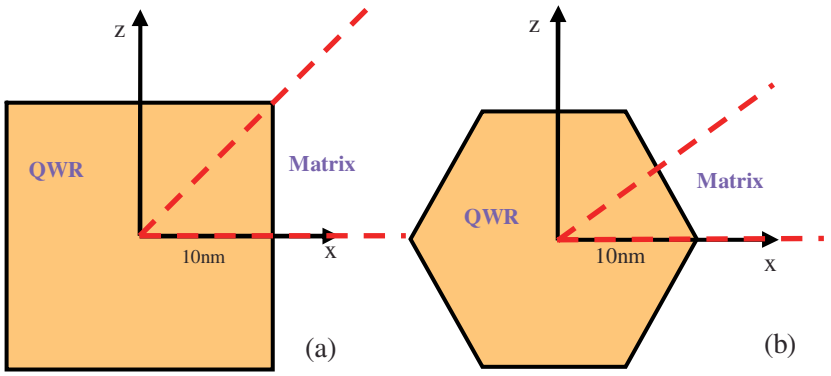

Fig. 3 (online colour at: www.pss-b.com) A square QWR in GaAs (a) and a hexagon QWR in AlN (b). The dashed lines show where the responses are calculated.

prediction for the purely elastic QWR case [11, 12]. We also note that for the elliptical QWR case, the horizontal strain γ_{xx} (the small x-component) based on the inhomogeneity model can be much different than those based on the inclusion model. Perhaps the most important feature is on the difference of the electric fields (in units of 10^7 V/m) in the InAs/GaAs(111) system. It is observed that the electric field difference based on the inclusion and inhomogeneity models can be more than one order of the magnitude (Table 4). This special feature has not been reported in any previous investigation and will be discussed again in the following two examples.

4.2 Example 2. Square QWR in GaAs and hexagon QWR in AlN

The second example is for a square QWR in GaAs and a hexagonal QWR in AlN (Fig. 3) where the induced strain and electric fields are presented along the horizontal and diagonal (inclined in hexagon) lines (dashed lines in Fig. 3).

Shown in Figs. 4 and 5 are the hydrostatic strain ($\gamma_{xx} + \gamma_{zz}$) along both horizontal and diagonal lines in both InAs/GaAs(001) and InAs/GaAs(111). These results are similar to those for the InAs/GaAs QWR

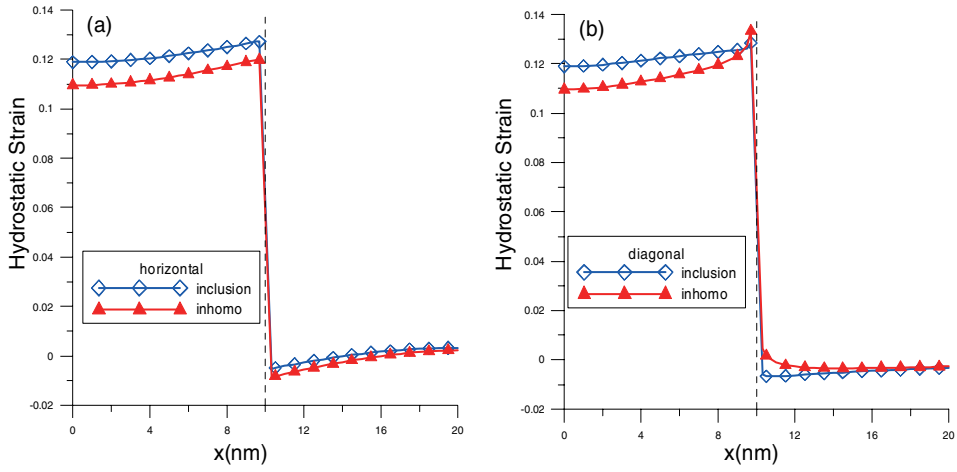

Fig. 4 (online colour at: www.pss-b.com) Hydrostatic strains ($\gamma_{xx} + \gamma_{zz}$) in a square QWR InAs/GaAs(001) along the horizontal (a) and diagonal (b) lines as defined in Fig. 3.

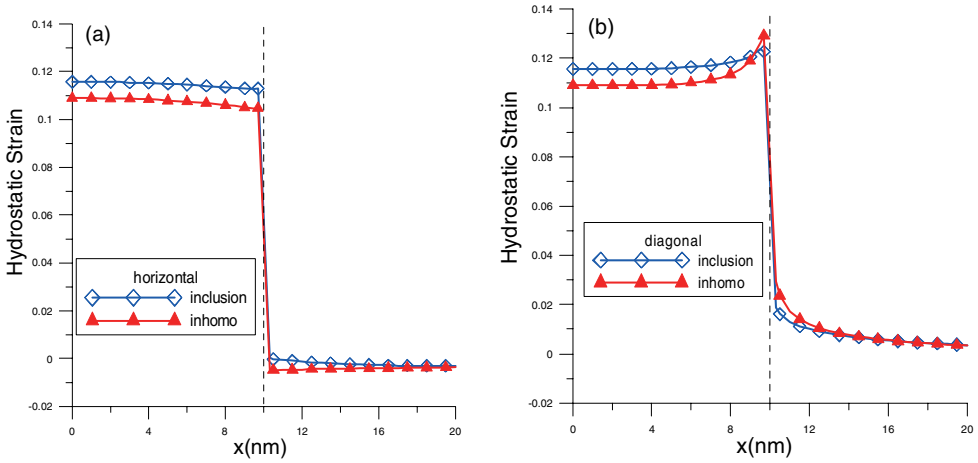

Fig. 5 (online colour at: www.pss-b.com) Hydrostatic strains ($\gamma_{xx} + \gamma_{zz}$) in a square QWR InAs/GaAs(111) along the horizontal (a) and diagonal (b) lines as defined in Fig. 3.

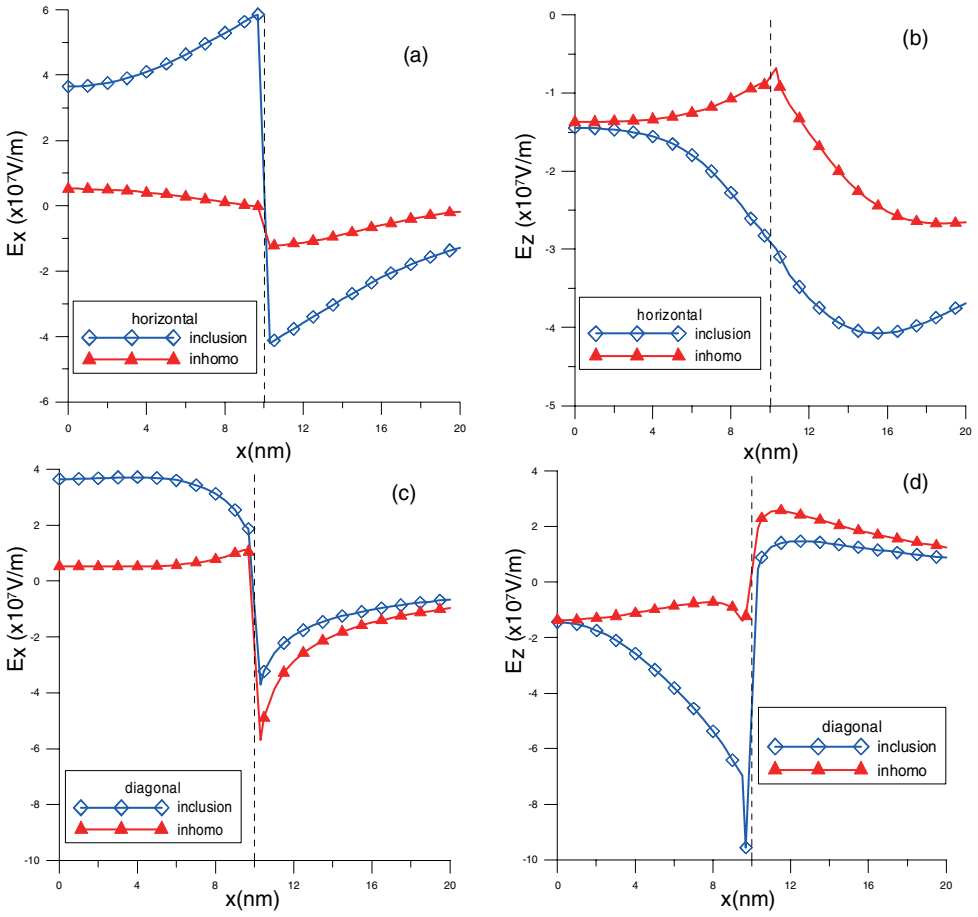

Fig. 6 (online colour at: www.pss-b.com) E_x (a) and E_z (b) along the horizontal line, and E_x (c) and E_z (d) along the diagonal line, in square QWR InAs/GaAs(111).

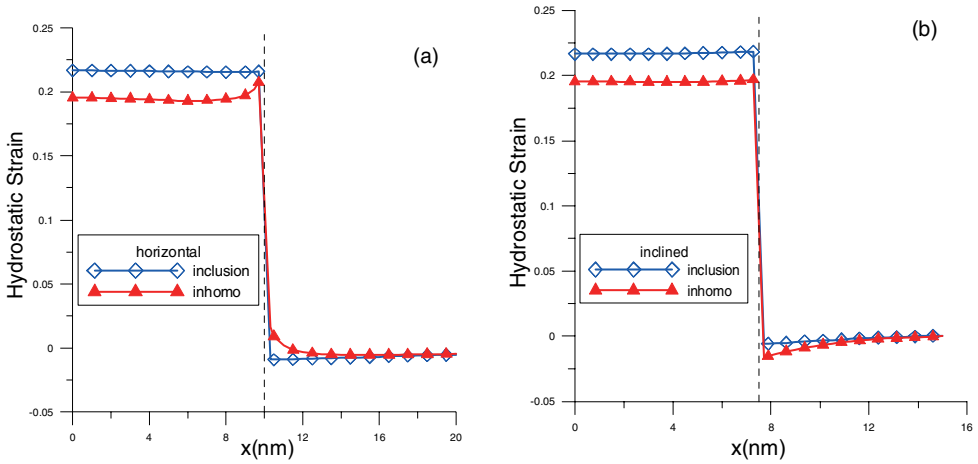

Fig. 7 (online colour at: www.pss-b.com) Hydrostatic strains ($\gamma_{xx} + \gamma_{zz}$) in hexagon QWR InN/AlN(0001) along horizontal (a) and inclined (b) lines.

with trapezoidal cross-section [12]. In general, the elastic strain fields inside the QWR are much larger than those in the substrate and the difference in the strain fields based on the inhomogeneity and inclusion models is apparent, particularly within the QWR.

It has been well-known that while there is no induced electric field in the InAs/GaAs(001) system, large electric fields can be observed in QWs, QWRs, and QDs (111) systems [19, 20]. Here in Fig. 6 we show for the first time that the induced electric fields along the horizontal and diagonal lines in InAs/GaAs(111) of a square QWR can be large and that the difference of the electric fields based on the inclusion and inhomogeneity models can be significant, especially within the QWR. In other words, electric fields in the InAs/GaAs(111) orientation should not be neglected, and should be considered using the inhomogeneity model as the simple inclusion model could be completely wrong. Furthermore, for the induced electric field, its magnitude both inside and outside the QWR are comparable, in contrast to the corresponding strain field featured in Figs. 4 and 5.

Figure 7 shows the hydrostatic strain in InN/AlN(0001) along the horizontal and inclined lines. Similar to the hydrostatic strain in the InAs/GaAs system, we observed that, outside the QWR, both the inclu-

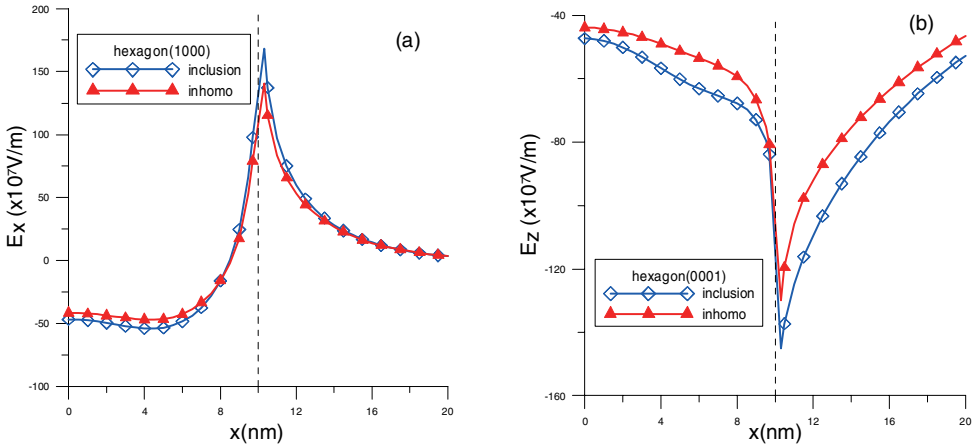

Fig. 8 (online colour at: www.pss-b.com) E_x in InN/AlN(1000) (a) and E_z in InN/AlN(0001) (b) along the horizontal line.

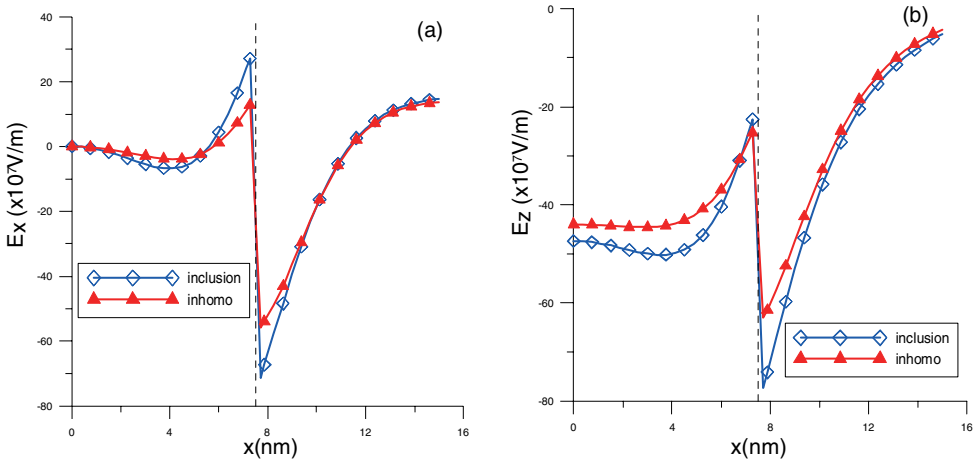

Fig. 9 (online colour at: www.pss-b.com) E_x (a) and E_z (b) in InN/AlN(0001) along the inclined line.

sion and inhomogeneity models predict similar results, with their magnitudes outside being also much smaller than those inside the QWRs. However, near the interface between the QWR and substrate, apparent differences can be observed. Furthermore, for the hydrostatic strain inside the QWR, the inclusion model predicts a higher value than the inhomogeneity model does (about 11%). For the InN/AlN(1000), the hydrostatic strain distribution is similar.

Figure 8 shows the electric field distribution along the horizontal line for both InN/AlN(0001) and (1000). For orientation (0001), the only non-zero E-field is E_x whilst for (1000), we have only E_z. It is observed from Fig. 8 that the inclusion model predicts very close results as compared to those based on the inhomogeneity one (particularly for E_x in Fig. 8a), except for the points close to the interface where the E-field experiences a shape change, resulting in different values based on different models.

Shown in Figs. 9 and 10 are the E-fields E_x and E_z along the inclined line in both InN/AlN(0001) and (1000). It is noted that along the inclined line, both E_x and E_z are different from zero, as compared to Fig. 8 where one of the electric components is zero. Similar to Fig. 8, the results predicted by the simple inclusion model are somewhat more reliable by comparison with those based on the inhomogeneity model; however, inside the QWR or close to the interface between the QWR and substrate, the inhomogeneity should be employed.

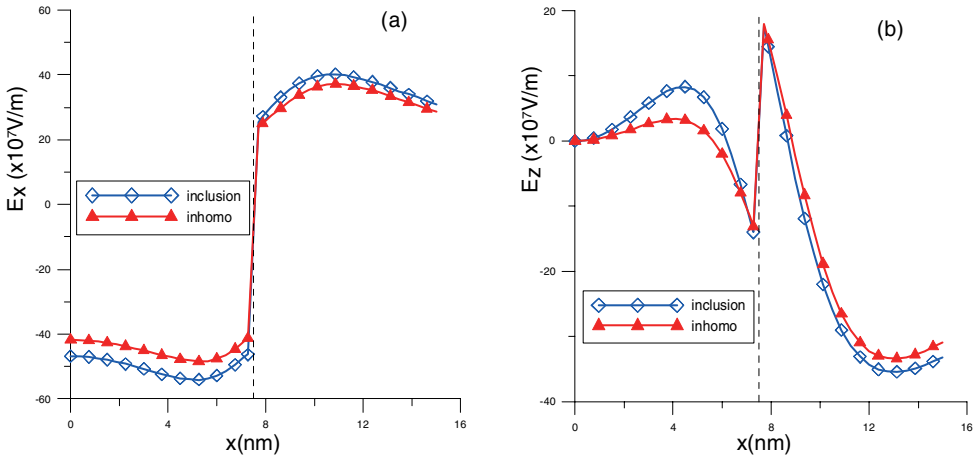

Fig. 10 (online colour at: www.pss-b.com) E_x (a) and E_z (b) in InN/AlN(1000) along the inclined line.

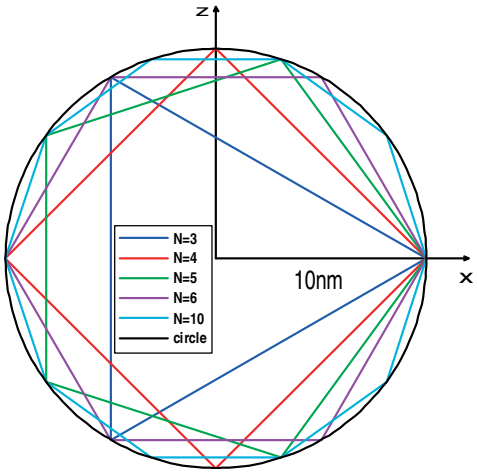

Fig. 11 (online colour at: www.pss-b.com) Polygons with sides $n = 3, 4, 5, 6, 10$ and infinity (circle).

4.3 Example 3. QWRs of different polygonal shapes

In this example, we study the induced E-fields inside and outside a polygonal QWR with different sides ($n = 3, 4, 5, 6, 10$, and infinity), a model used before for the corresponding corner singularity study [21]. The model is shown in Fig. 11 with the E-fields being calculated along the horizontal x-axis. Only the results from the inhomogeneity models InAs(111)/GaAs(111), InN(0001)/AlN(0001), and InN(1000)/AlN(1000) are presented.

Figure 12 shows that inside and outside the QWR of InAs/GaAs(111), both E-field components are nonzero along the horizontal x-axis and that just as for the second example, the magnitudes of the E-fields are comparable both inside and outside the QWR. We also observe that the results from the regular triangle and square QWRs are completely different from the other polygonal QWRs. This can be seen more clearly from Table 7 where the E-fields at the center of the polygons are listed. It is obvious that the signs of E_x and E_z, are respectively the same for both triangle and square QWRs, which, however, have opposite signs as compared to those in other polygons. Furthermore, while the central values of the E-fields are very small for the triangle QWR, the E_z component in square QWR are much larger than those in other polygon (50–100% larger). These distinguished features are directly associated the

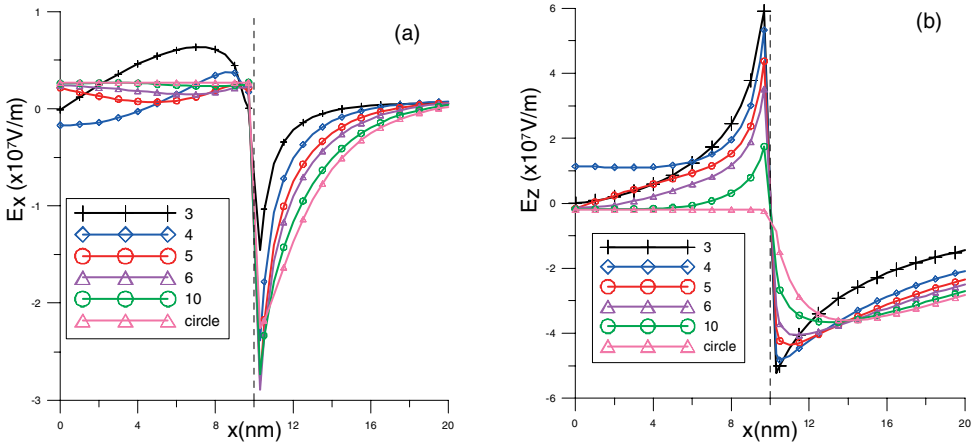

Fig. 12 (online colour at: www.pss-b.com) E_x (a) and E_z (b) in InAs/GaAs(111) along the horizontal line for $n = 3, 4, 5, 6, 10$, and infinity (circle).

Table 7 Electric fields at the center of the polygonal QWRs of InAs/GaAs(111).

polygon sides/fields	E_x (MV/m)	E_z (MV/m)
3	**−0.0071**	**0.0012**
4	**−0.1701**	**1.1285**
5	0.2182	−0.1546
6	0.2396	−0.1430
10	0.2613	−0.1851
circle	0.2689	−0.1902

geometric shape: while the triangle and square are very different to each other, a polygon with sides ≥5 is closer to a circular shape than both triangle and square (Fig. 11).

Figure 13 shows the E-field along the horizontal axis in InN/AlN(1000) and (0001). Due to the symmetric property of the problem the only nonzero component is E_x in (1000) orientation and E_z in (0001) orientation. It is noted that: (1) There is a sharp change in the E-field at the geometric corner point (x = 10 nm), (2) The trend of the field variation in triangle QWR is completely different to those in other polygons; and (3) At the center of the polygons, the E-field of the square is much larger than those in other polygons where the results are very close to each other (Table 8) except for the square QWR. The difference of the E-field magnitude at the center between square and other polygons is about 25%.

5 Concluding remarks

In the paper, an accurate BEM modeling is proposed for the strain and electric field analysis in QWR structures. Constant elements are employed to discretize the interface between the QWR and substrate with the integrand being analytically carried out utilizing close-form Green's functions for anisotropic piezoelectric solids. The elastic and piezoelectric response at any location can be predicted based on the inclusion and inhomogeneity models. From our study, some important features are observed, with those for the strain field being consistent to recent published results: (1) In the substrate and far away from the QWR, both the inclusion and inhomogeneity models predict nearly the same strain field. In other words, the simple inclusion model can be safely applied if one would like to have a quick estimation of the far-field strain. (2) For points inside or close to the QWR, the strain difference between the two models can be as high as 10% for the test structures, which can result in strong variations of the confined electronic

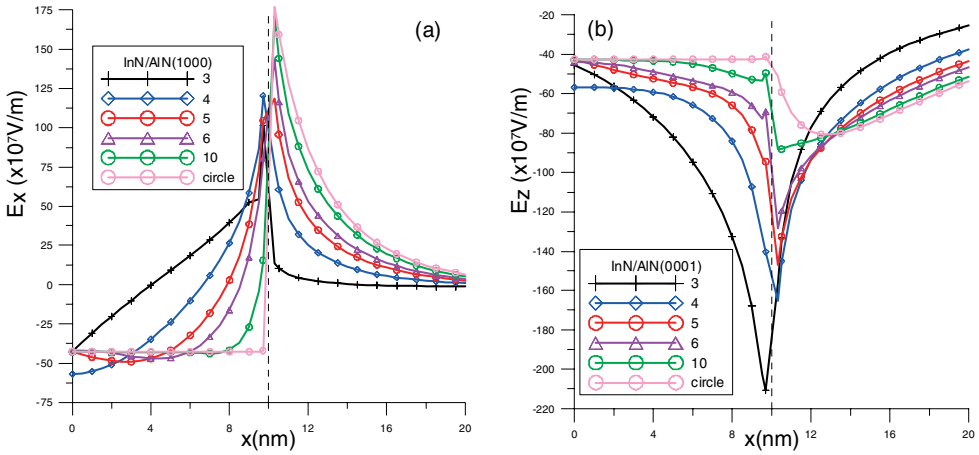

Fig. 13 (online colour at: www.pss-b.com) E_x (a) in InN/AlN(1000) and E_z (b) in InN/AlN(0001) along the horizontal line for n = 3, 4, 5, 6, 10, and infinity (circle).

Table 8 Electric fields ($\times 10^7$V/m) at the center of the polygonal QWRs of InN/AlN.

polygon sides/fields	E_x in (1000)	E_z in (0001)
3	–42.33	–45.74
4	**–56.89**	**–56.89**
5	–42.86	–43.00
6	–41.73	–43.96
10	–42.63	–42.76
circle	–42.66	–42.66

states. (3) While the magnitude of strain inside the QWR is much larger than that outside, the electric fields have the same magnitudes both inside and outside the QWR. (4) While the relative difference in the electric fields based on both inclusion and inhomogeneity models can be large in the InAs/GaAs(111) system, that in InN/AlN is relatively small. In other words, for InN/AlN where the electric field is large, the simple inclusion model could be employed for the calculation of the induced electric field. This is particularly true as the difference in the electric field based on both models could be small compared to the difference that arises due to the uncertainty in the material constants used [22]. (5) It is also observed that the electric fields in the QWR depend strongly on the QWR geometry shape; The electric field in triangular and square QWRs is different from those in the polygons made of more than 4 sides.

Acknowledgement This work was supported in part by AFOSR FA9550-06-1-0317.

References

[1] M. Grundmann, O. Stier, and D. Bimberg, Phys. Rev. B **52**, 11969 (1995).
[2] J. D. Eshelby, Proc. R. Soc. Lond. A **241**, 376 (1957).
[3] J. D. Eshelby, Prog. Solid Mech. **2**, 89–140 (1961).
[4] T. Mura, Micromechanics of Defects in Solids, 2nd revised ed. (Kluwer Academic Publishers, 1987).
[5] D. A. Faux, J. R. Downes, and E. P. O'Reilly, J. Appl. Phys. **80**, 2515 (1996).
[6] J. H. Davies, J. Appl. Phys. **84**, 1358 (1998).
[7] C. Q. Ru, Proc. R. Soc. Lond. A **456**, 1051 (2000).
[8] F. Glas, phys. stat. sol. (b) **237**, 599 (2003).
[9] E. Pan, J. Mech. Phys. Solids **52**, 567 (2004).
[10] R. Maranganti and P. Sharma, in: Handbook of Theoretical and Computational Nanotechnology, edited by M. Rieth and W. Schommers (American Scientific Publishers, 2006), chap. 118.
[11] B. Yang and E. Pan, J. Appl. Phys. **92**, 3084 (2002).
[12] E. Pan, F. Han, and J. D. Albrecht, J. Appl. Phys. **98**, 013534 (2005).
[13] D. M. Barnett and J. Lothe, phys. stat. sol. (b) **67**, 105 (1975).
[14] E. Pan, Eng. Anal. Bound. Elem. **23**, 67 (1999).
[15] C. A. Brebbia and J. Dominguez, Boundary Elements: An Introductory Course (Computational Mechanics Publications, Southampton, 1992).
[16] T. C. T. Ting, Anisotropic Elasticity (Oxford University Press, Oxford, 1996).
[17] E. Pan, Proc. R. Soc. Lond. A **458**, 181 (2002).
[18] E. Pan, J. Appl. Phys. **91**, 3785 (2002).
[19] E. Pan, J. Appl. Phys. **91**, 6379 (2002).
[20] D.L. Smith, Solid State Commun. **57**, 919 (1986).
[21] E. Pan and X. Jiang, Mech. Res. Commun. **33**, 1 (2006).
[22] U. M. E. Christmas, A. D. Andreev, and D. A. Faux, J. Appl. Phys. **98**, 073522 (2005).

